Increasing ORR Kinetics of Pd/C via Ag and Cu Integration: A Robust and Promising Catalyst for Oxygen Reduction Reaction

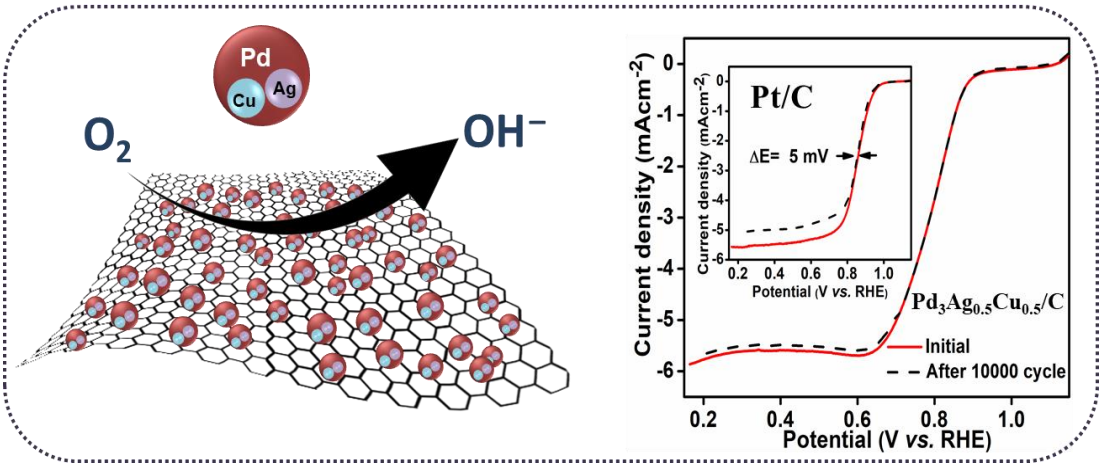

In this chapter, we studied the synthesis of carbon-supported $Pd_3Ag_{0.5}Cu_{0.5}$ NPs along with different PdCu and PdAg NPs with varied atomic ratios via a typical solvothermal method and evaluated for ORR activities. The $Pd_3Ag_{0.5}Cu_{0.5}/C$ was highly active and more stable toward ORR than the other reported NPs. Adding Cu and Ag alters the Pd's lattice environment, modifies its electronic environment and eventually improves the active sites for ORR. The experimental procedures for the synthesis, characterization techniques, and electrocatalytic measurements of the samples were described in Chapter 2.

3.1. Introduction

Development of eco-friendly sustainable energy to compensate for the depletion of fossil fuels and mitigate CO_2 emission has brought high demand for non-conventional energy conversion systems, such as fuel cells (FCs) [1, 2]. Heat and water, being only byproducts of a FC, represent them as a promising alternative technology with tremendous potential for large scale production with high efficiency towards clean energy production [3]. The FCs can efficiently convert chemical energy stored in biomass-derived fuels for example, H_2O, methanol, etc. to electrical energy by complementarily carrying out a cathodic reaction by using oxygen as an oxidant [4, 5]. In the other hand, the slow kinetic nature of ORR restricts the productivity of the FCs [6]. Although Pt based electrocatalysts are high-performance catalysts towards ORR but their high cost and poor durability make the commercialization of such systems difficult [7-9].

There is an ongoing effort to replace Pt-based electrocatalyst. Pd has been identified to show similar activity towards ORR in alkaline medium [10, 11]. It is, therefore, highly desirable and need of the hour to develop high-efficiency Pd-based electrocatalysts with a substantially enhanced ORR performance. Since Pd is also considered to be a precious metal, addition of d-block transition metals in order to reduce the economic stress on Pd alone and also synergistically improve the catalytic properties is a constructive approach to meet the gap of commercialization [12, 13].

Studies have shown that the strong interaction between the Pd and intermediates which contain oxygen such as $^*O$, $^*OH$ and $^*OOH$ conventionally cause sluggish kinetics towards ORR [14]. Metals such as Ag, Cu, Ni, Co, etc., that bind strongly with oxygen lowers the binding nature of oxygen towards the noble metals such as Pt and Pd, which results in improved ORR activity [15-18]. From computational studies, it has been stated that an upward shift of the d states of metals will cause an upshift of the antibonding states; this ultimately causes unfavourable elimination of O and OH species adsorbed on the surface due to stronger metal-oxygen bonds [19]. Tang *et al*. found that the activity enhancement of Pd/Cu NPs was due to transfer of charge from Cu to Pd, which resulted in rise of the d band of Cu while lowering that of Pd, causing stronger oxygen bindings with Cu sites rather than Pd, making more Pd sites available for catalysis [20]. The surface strain caused from the distortion of crystal lattice from the ideal arrangement provides an alternative approach to maximise the catalytic behaviour of the electrocatalyst [21]. Moreover, the Pd-based catalysts show moderate oxygen binding energy, which

falls in accordance with the Sabatier principle for catalysis [19]. Additionally, the inclusion of conductive carbon such as graphene as a support which has excellent electrical conductivity and facilitates relatively uniform dispersion of metal components on the surfaces enhances the overall activity of the catalyst [22-24]. Karuppasamy *et al.* reported reduced graphene oxide (rGO) nanosheet-supported PdAg NPs, which showed excellent electrochemical activity towards ethanol oxidation and ORR [25]. In another work, it was found that epitaxially growing of the Au NPs on Pd metallene led to epitaxial heterointerface between Au and Pd causing modification in the electronic structure of Pd, raising its oxidation potential for better stability [26].

Based on these standpoints, a series of graphene supported Ag and Cu doped Pd electrocatalysts are synthesized. Among them, $Pd_3Ag_{0.5}Cu_{0.5}$/C showed significant ORR activity with appreciable durability. It is anticipated that a new environment is generated while introducing Ag and Cu in Pd which can enhance O-O bond rupturing and helps in oxygen reduction. The dispersion of $Pd_3Ag_{0.5}Cu_{0.5}$ in the graphene enhanced the conductivity and prevented the metals from agglomerating in alkaline medium. Additionally, the superior performance of the nanomaterials could result from the robust anchoring of $Pd_3Ag_{0.5}Cu_{0.5}$ NPs to the carbon substrate and reduced the electrochemical degradation of carbon.

3.2. Results and Discussion

3.2.1. Characterizations of the hybrid NPs

The XRD patters of $Pd_3Ag_{0.5}Cu_{0.5}$/C, Pd_3Ag/C, Pd_3Cu/C, $PdAg_3$/C, $PdCu_3$/C and Pd/C are depicted in Figure 3.1a. The characteristic peaks of the Pd, such as Pd (111), (200), (220), and (311) were observed in all the samples; this confirms the presence of Pd. Compared to commercial Pd/C, the diffraction peaks of all catalysts were slightly broad and shifted. This is due to the introduction of different size metal atoms i.e., Cu and Ag into the Pd unit cell. In $PdCu_3$/C and $PdAg_3$/C, we observed highly shift towards positive and negative 2θ value, respectively due to lattice contraction and lattice expansion of Pd lattice and this observation is consistent with the lower and higher atomic radius of Cu and Ag, respectively to that of Pd. A peak observed for all the NPs at ~26º corresponds to the (002) plane of graphene NPs.

To identify the metal content on the graphene support, a TGA analysis was carried out in an air atmosphere and presented in Figure 3.1b. A significant weight loss was seen at 340 °C due to the conversion of carbon to CO_2. The weight loss reaches a stable point at ~ 580 °C, with a ~20% residue equivalent to the total amount of metal loaded onto the graphene substrate. EDS and elemental mapping analysis, displayed in Figure 3.2, identify the presence Pd, Ag, Cu and C with a uniform distribution. The atomic ratios of Pd, Ag, and Cu are 12.09%, 1.766% and 1.964%, respectively, consistent with the results taken with the theoretically calculated value, i.e., 6:1:1 ratio. The elemental composition spectra for Pd, Ag, Cu and C are consistent with the calculation of the synthesized compounds. Additionally, the total metal loading of $Pd_3Ag_{0.5}Cu_{0.5}$ (~20%) over the carbon support (~80%) obtained from EDX analysis matches well with the TGA findings.

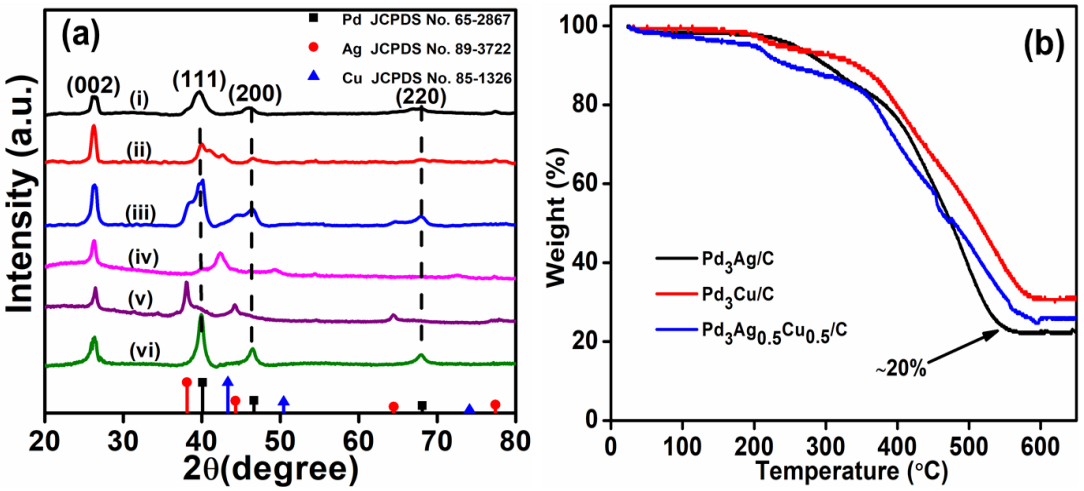

Figure 3.1: (a) p-XRD patterns of (i) $Pd_3Ag_{0.5}Cu_{0.5}$/C, (ii) Pd_3Cu/C, (iii) Pd_3Ag/C, (iv) $PdCu_3$/C, (v) $PdAg_3$/C and (vi) Pd/C, (b) TGA profile of $Pd_3Ag_{0.5}Cu_{0.5}$/C, Pd_3Ag/C and Pd_3Cu/C in air atmosphere.

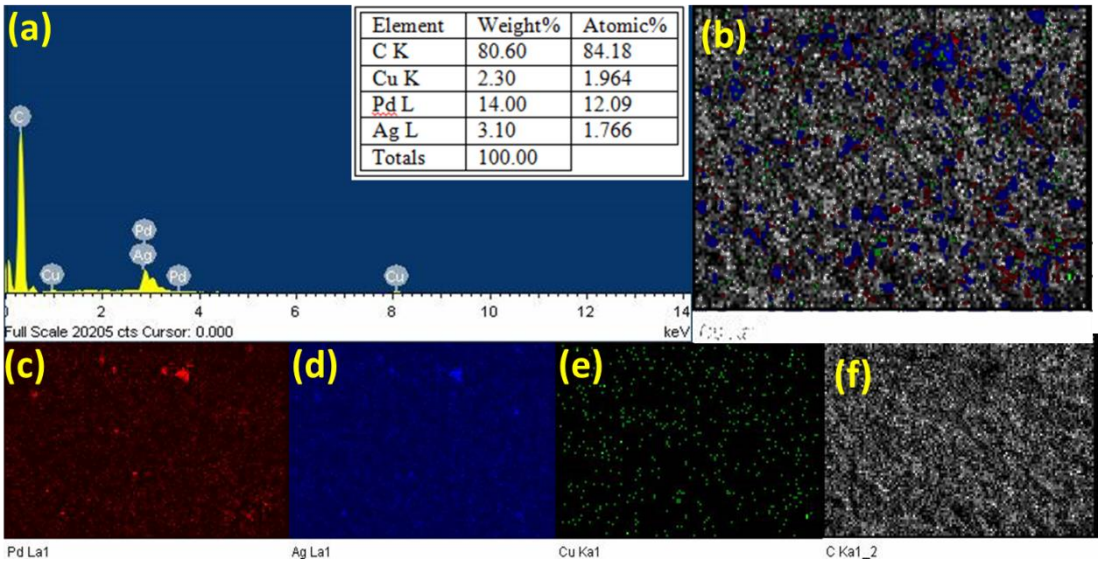

Figure 3.2: EDX pattern of $Pd_3Ag_{0.5}Cu_{0.5}/C$; (a) EDX spectrum; inset shows the table for elemental composition, (b) The overlayer image of C, Pd, Ag and Cu, (c)-(f) elemental maps for individual Pd, Ag, Cu, and C, respectively.

The morphology of the as-synthesized $Pd_3Ag_{0.5}Cu_{0.5}/C$ was carried out by TEM analysis presented in Figure 3.3. The $Pd_3Ag_{0.5}Cu_{0.5}$ NPs appear dark on the graphene support and the NPs are uniformly distributed over the graphene support with an average diameter of 5-6 nm based on a statistical analysis of more than 35 NPs (Figure 3.3a). The uniform distribution of NPs with no significant agglomeration indicates a stronger interaction between $Pd_3Ag_{0.5}Cu_{0.5}$ and the graphene surface (Figure 3.3b). The interaction between metal and support can impact the catalytic performance of ORR by generating metal support interaction [3]. The incorporation of Ag and Cu induces strain on the Pd due to lattice mismatch, and modifying the electronic structure via charge transfer processes. The HRTEM image of the $Pd_3Ag_{0.5}Cu_{0.5}/C$ in Figure 3.3c contains lattice fringes with d-spacings of 0.225, 0.235 and 0.208 nm, ascribed to the (111) facet of Pd, Ag and Cu, respectively. It is important to note that these NPs may promote ultrahigh atom utilization, improve the efficiency of ultrahigh utilization of metal atoms and which will enhance the catalytic activity [27]. Additionally, the red dotted line in the TEM images are discontinued lattice fringes in the NPs, highlighting the presence of numerous defects. These defects are generally believed to enhance the active site exposure, which is advantageous for electrocatalytic activity [28]. The SAED pattern (Figure 3.3d) revealed the details of the polycrystalline nature, and the concentric rings could be identified as

reflections from the (111), (220), and (311) planes of *fcc* Pd, which is in agreement with the XRD findings.

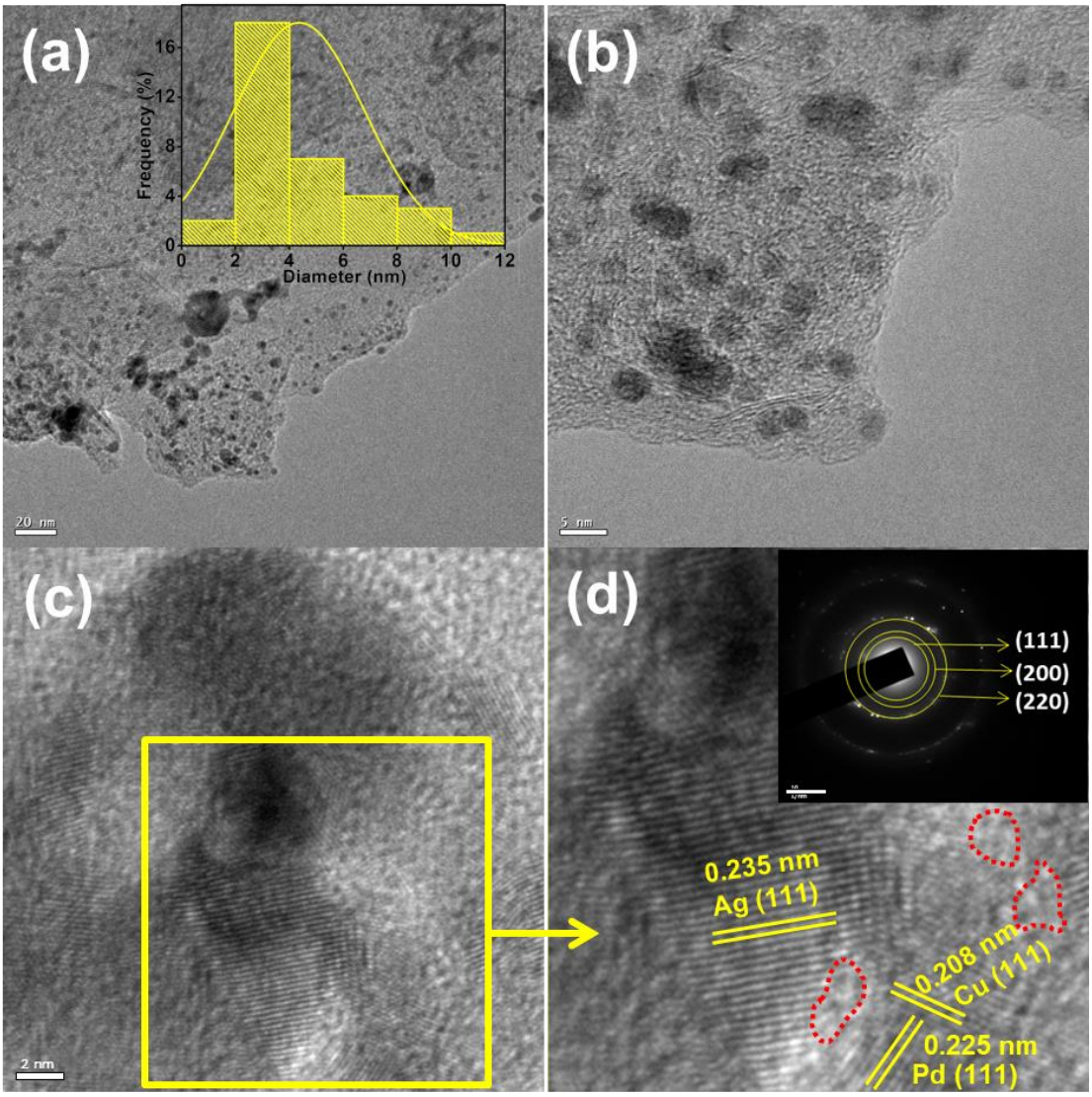

Figure 3.3: (a) TEM image (inset: corresponding size distributions histogram of $Pd_3Ag_{0.5}Cu_{0.5}$ measured from the TEM images), (b-c) HRTEM image, and (d) the magnified HRTEM image enlarged from region marked by square in (c) and the red dotted area denote the defects on the surface of the NPs (inset: selected area diffraction (SAED) pattern for $Pd_3Ag_{0.5}Cu_{0.5}$/C).

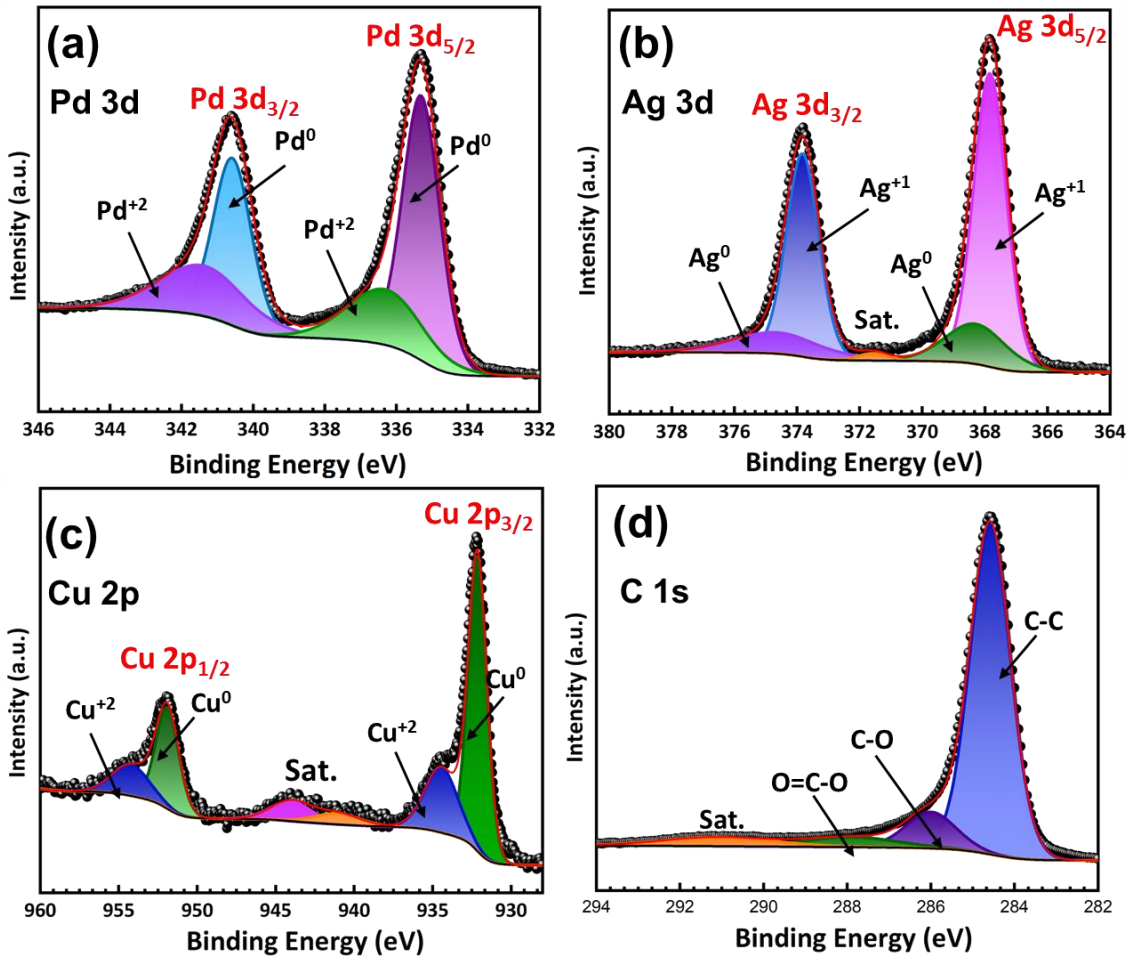

Figure 3.4: High resolution XPS spectra of (a) Pd 3d, (b) Ag 3d, (c) Cu 2p and (d) C 1s of $Pd_3Ag_{0.5}Cu_{0.5}$/C.

XPS measurements of the $Pd_3Ag_{0.5}Cu_{0.5}$/C presented in Figure 3.4 were performed to investigate the valence states and electronic structure of elements. The high-resolution spectrum of Pd 3d peaks corresponds to Pd $3d_{5/2}$ and $3d_{3/2}$, respectively, where peaks at 335.5 and 341.0 eV were assigned to Pd^0 and peaks at 337.3 and 342.6 eV were assigned to Pd^{2+} (Figure 3.4a) [29,30]. In the region of Ag 3d (Figure 3.4b), the $3d_{5/2}$ peak at 368.8 eV and the $3d_{3/2}$ peak at 377.4 eV were indicative of the existence of Ag^0, along with a well separated spin-orbit components (Δ_{metal} = 6.0 eV), indicates a peak at 367.9 eV for $3d_{5/2}$ and one at higher energy side 373.9 eV for $3d_{3/2}$ indicative of the existence of Ag^+ [31-33]. Similarly, the Cu 2p spectrum showed peaks around 932.1 and 951.8 eV, with distinguished spin-orbit component (Δ_{metal} = 19.75 eV) which confirms the $2p_{3/2}$ and $2p_{1/2}$ bands of metallic Cu species, respectively shown in Figure 3.4c and two other weak peaks were observed at 934.9 and 954.8 eV which is due to Cu^{2+}, another one at 932.5eV due to

the presence of Cu^{+}, indicated that there is Cu_2O as shell of NP presence with oxidized Cu^{+2}. Along with two very weak satellite peaks were also observed at around 940 and 944 eV [34, 35]. The C 1s spectrum consists of three main peaks at binding energies of 284.6, 286.0 and 288.0 eV. The peak around 284.6 eV was a typical nature of graphitic carbon, one at 286.0 eV could be indexed to the C–O functional group in graphene and another one at 288.5 eV for O=O-C (Figure 3.4d) [36]. The binding energy values corresponding to various elements from of high resolution XPS spectrum of $Pd_3Ag_{0.5}Cu_{0.5}$/C presented in table 3.1. Notably, the results showed that the Pd, Ag, Cu is mainly in the metallic state, confirming the complete reduction of Pd, Ag and Cu, while the appearance of few weak metals oxidized peaks is attributed to the surface oxidation of metal species in air.

Table 3.1. Binding energy values corresponding to various elements from high resolution XPS spectrum of $Pd_3Ag_{0.5}Cu_{0.5}$/C.

Elements	**Peak assignment**		**Peak position (eV)**
C	C-C		284.6
	C-O		286.0
	O=C-O		288.5
Pd	Pd $3d_{3/2}$	Pd^0	341.0
		Pd^{2+}	342.6
	Pd $3d_{5/2}$	Pd^0	335.5
		Pd^{2+}	337.3
Ag	Ag $3d_{3/2}$	Ag^0	377.4
		Ag^{+}	373.9
	Ag $3d_{5/2}$	Ag^0	368.08
		Ag^{+}	367.9
Cu	Cu $2p_{1/2}$	Cu^0	951.8
		Cu^{2+}	954.8
	Cu $2p_{3/2}$	Cu^0	932.1
		Cu^{+}	932.5
		Cu^{2+}	934.9

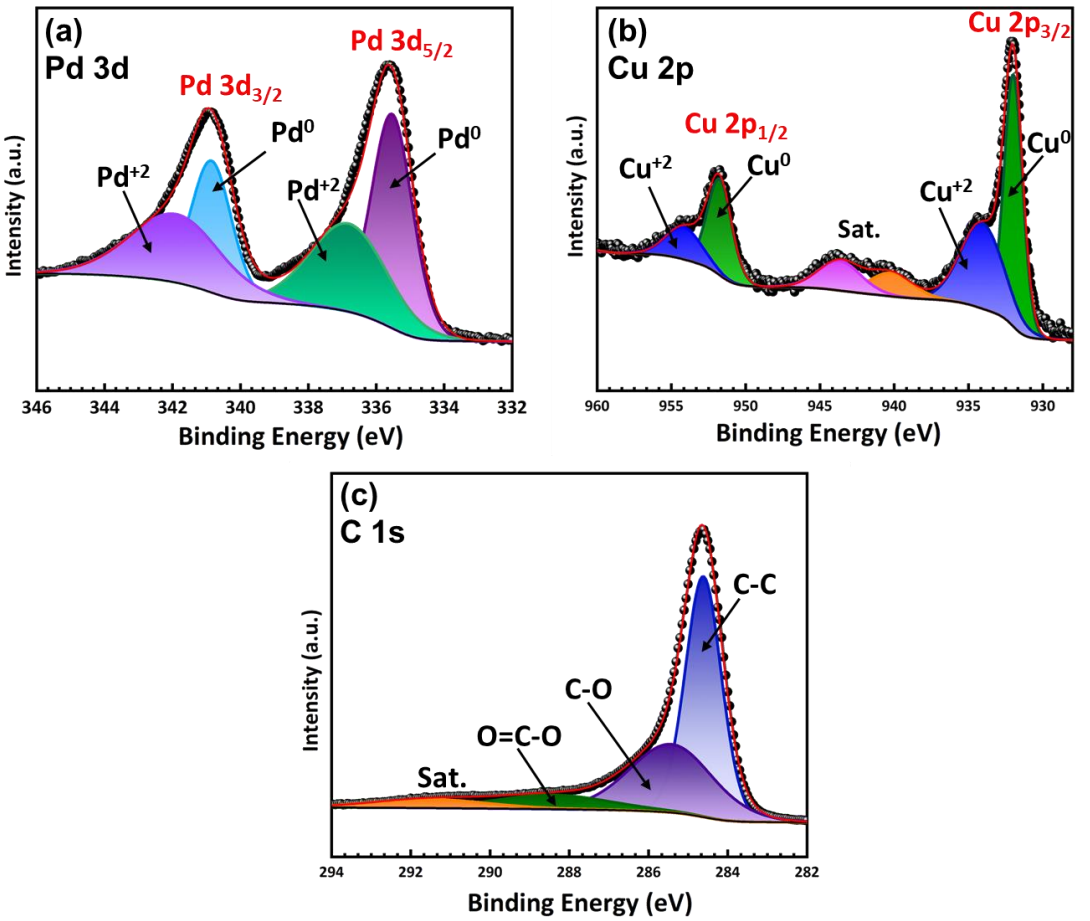

Figure 3.5: High resolution XPS spectra of Pd_3Cu/C: (a) Pd 3d, (b) Cu 2p and (c) C 1s.

Furthermore, the high resolution XPS spectra of Pd_3Cu/C and Pd_3Ag/C (Figure 3.5 and 3.6) depicts the presence of C, Pd, and Cu in Pd_3Cu/C and C, Pd, and Ag in Pd_3Ag/C, respectively. Upon deconvolution and fitting of all peaks were found to possess nearly identical binding energies with slight shifting relative to $Pd_3Ag_{0.5}Cu_{0.5}/C$, implicating successful formation of Pd_3Ag/C and Pd_3Cu/C, respectively. Notably, the slight shifting indicates the incorporation of third metal in Pd_3Ag/C or Pd_3Cu/C and changes the electronic environment.

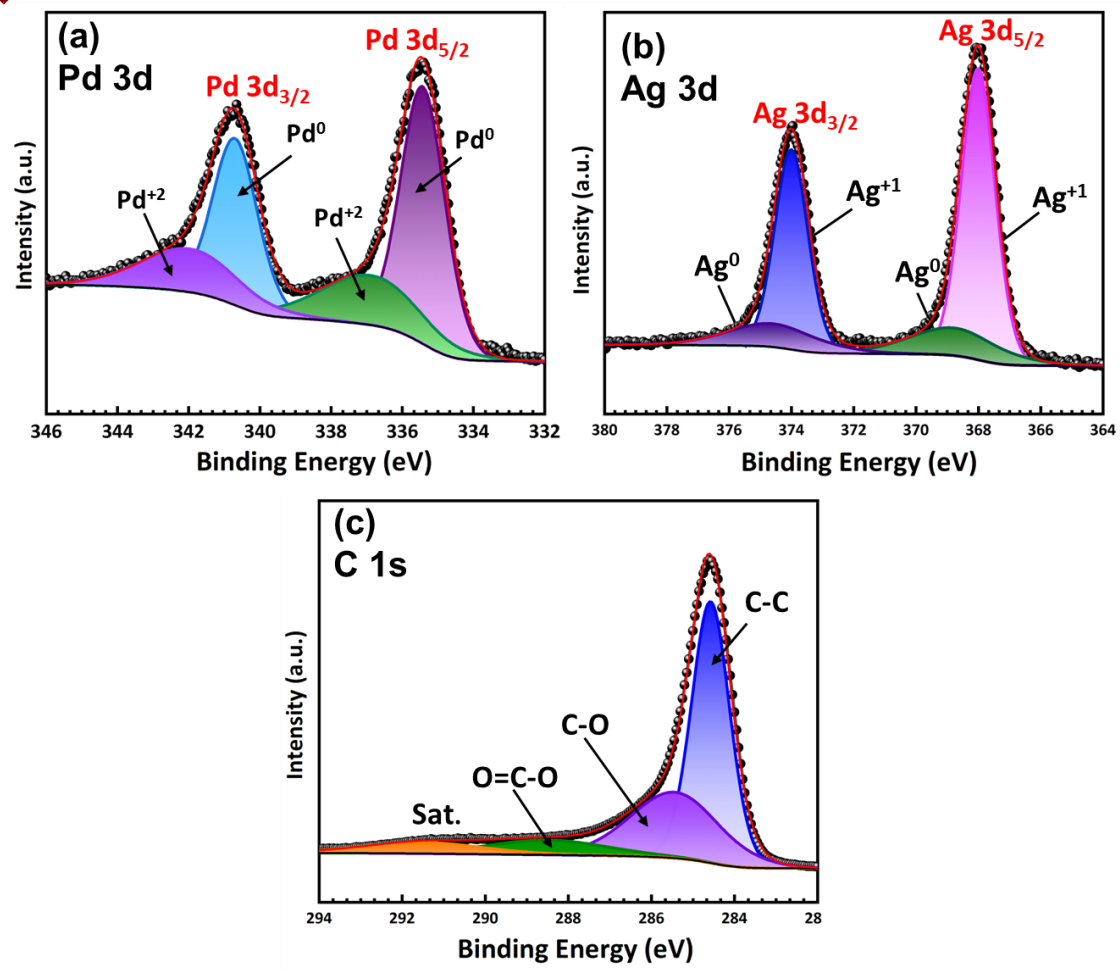

Figure 3.6: High resolution XPS spectra of Pd_3Ag/C: (a) Pd 3d, (b) Ag 3d, and (c) C 1s.

3.2.2. Electrocatalytic activity towards ORR

For investigating the ORR performance of the synthesized catalysts, as discussed in Chapter 2, CV measurements were done in N_2 and O_2-saturated electrolytes (Figure 3.7a). A sharp and distinct reduction peak was observed in the O_2-saturated electrolyte, indicating the catalyst is active towards ORR. In order to investigate the kinetics of the ORR process, electrochemical activity under hydrodynamic environments was assessed. The LSV curves were plotted from 0.2-1.2 V (*vs.* RHE) at a sweep rate of 10 mVs^{-1} with rotating speeds of 400-3600 rpm and presented in Figure 3.7b. With the increase in the rotating rate, the current density increases, suggesting a diffusion control process. The electron transfer significantly influences the catalytic performance of the materials is significantly influenced by the number of electrons transfer (n) in the ORR process and it can be calculated by the Koutecky−Levich (K-L) equation (discussed in Chapter 2).

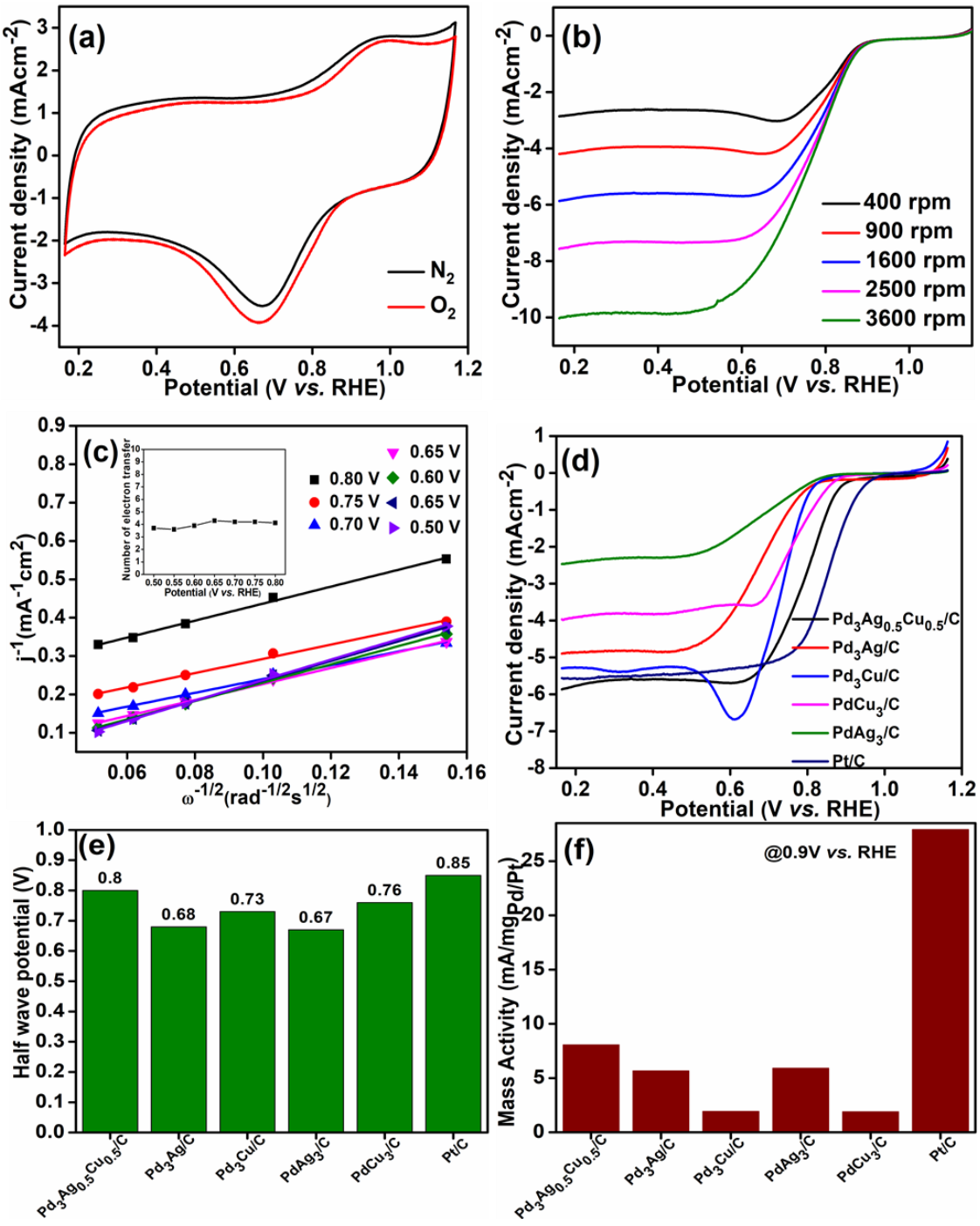

Figure 3.7: Electrochemical characterization of the catalysts: (a) CV curves of $Pd_3Ag_{0.5}Cu_{0.5}/C$ in 0.1 M KOH with N_2 and O_2 saturated atmosphere, (b) LSV curves of $Pd_3Ag_{0.5}Cu_{0.5}/C$ at 400-3600 rpm, (c) KL plot (inset: electron transfer number), (d) LSV curves of different electrocatalysts at a rotating speed of 1600 rpm, (e) half-wave potential ($E_{1/2}$) and (f) mass specific activity normalized to the mass loading of Pd/Pt on the electrocatalysts at different potentials obtained from LSV 1600 rpm.

The K−L plots at different potentials presented in Figure 3.7c showed a linear and parallel relationship, implying a first-order reaction toward concentration of dissolved oxygen. From the KL equation, the n was calculated and found to be ~4, indicating that O_2 was converted to OH^- directly by the $4e^-$ pathway. The direct $4e^-$ pathway is more favourable, whereas the indirect $2e^-$ pathway will produce H_2O_2, which possesses a high oxidation capacity and would speed up the corrosion of the catalysts [3, 37-39]. The comparison of LSV for all the catalysts in O_2-enriched 0.1 M KOH solution recorded at 10 mVs^{-1} scan rate with 1600 rpm rotation rate are presented in Figure 3.7d. The $Pd_3Ag_{0.5}Cu_{0.5}$/C exhibited the earliest onset (E_{onset}) and half wave potential ($E_{1/2}$) than the other catalysts. The highest diffusion-limited current density (j_m) was observed for $Pd_3Ag_{0.5}Cu_{0.5}$/C (−5.84 mA/cm^2) than other bimetallic counterparts, even higher than the benchmark Pt/C displayed good mass-transfer properties. The $E_{1/2}$ of the $Pd_3Ag_{0.5}Cu_{0.5}$/C (0.80 V) is 12, 7, 13 and 4 mV positive than the Pd_3Ag/C, Pd_3Cu/C, $PdAg_3$/C and $PdCu_3$/C, respectively (Figure 3.7e), revealing its superior electrocatalytic activity toward ORR in alkaline electrolyte. Moreover, more positive E_{onset} and $E_{1/2}$ than those of the Pd_3Cu/C, Pd_3Ag/C, $PdAg_3$/C, and $PdCu_3$/C, indicating that increased ORR activities of $Pd_3Ag_{0.5}Cu_{0.5}$/C at considerably lower overpotentials. The admirable ORR activity is mainly because the incorporation of Ag and Cu can induce lower adsorption energy of oxygen intermediate owing to the downshift of Pd *d*-band center and high atom utilization due to the smaller size of the NPs. Furthermore, mass activity (MA) is the essential parameter for evaluating catalyst performance and it is determined by normalizing corresponding LSV i.e.; 1600 rpm by total Pt or Pd mass loading of the catalysts. The MA plots at 0.90 V *vs.* RHE are presented in Figure 3.7f and it is observed that $Pd_3Ag_{0.5}Cu_{0.5}$/C displayed the highest MA. The highest MA value signifies highest total apparent ability of the catalysts. The electrochemical parameters of all the electrocatalysts were summarized in Table 3.2.

Table 3.2: Summary of onset potential (E_{onset}), half wave potential ($E_{1/2}$), limiting current density (j_m) and electrochemically active surface area (ECSA) of $Pd_3Ag_{0.5}Cu_{0.5}$/C, Pd_3Cu/C, Pd_3Ag/C $PdAg_3$/C, $PdCu_3$/C, and Pt/C toward ORR at 1600 rpm.

Electrocatalysts	**E_{onset} (V *vs.* RHE)**	**$E_{1/2}$ (V *vs.* RHE)**	**j_m (mA cm^{-2})**	**ECSA (m^2g^{-1})**
$Pd_3Ag_{0.5}Cu_{0.5}$/C	0.94	0.80	-5.84	146.5
Pd_3Cu/C	0.87	0.73	-5.29	137.3
Pd_3Ag/C	0.86	0.68	-4.89	2.08
$PdAg_3$/C	0.87	0.67	-2.46	4.01
$PdCu_3$/C	0.89	0.76	-3.96	66.2
Pt/C	0.98	0.85	-5.55	29.5

The electrocatalytic ORR analysis of Pd_3Cu/C, Pd_3Ag/C, $PdAg_3$/C and $PdCu_3$/C were also carried out using CV and RDE analysis. The obtained CV, LSV and their corresponding KL plots of Pd_3Cu /C and $PdCu_3$/C are presented in Figure 3.8. Similarly, for Pd_3Ag/C and $PdAg_3$/C, CV, LSV and their corresponding KL plots are shown in Figure 3.9. The n values of the electrocatalyst were calculated by using K–L equation over the potential window of 0.50 to 0.75 V *vs.* RHE (inset in Figure 3.8e, 3.8f, 3.9e and 3.9f) and found to be 2.5, 2.8, 2.1 and 3.2 for Pd_3Cu/C, Pd_3Ag/C, $PdAg_3$/C and $PdCu_3$/C, respectively. It implicates the difference in the extent of ORR toward OH^- and also signifies the electrocatalysts do not proceed via the direct $4e^-$ pathway for OH^- formation.

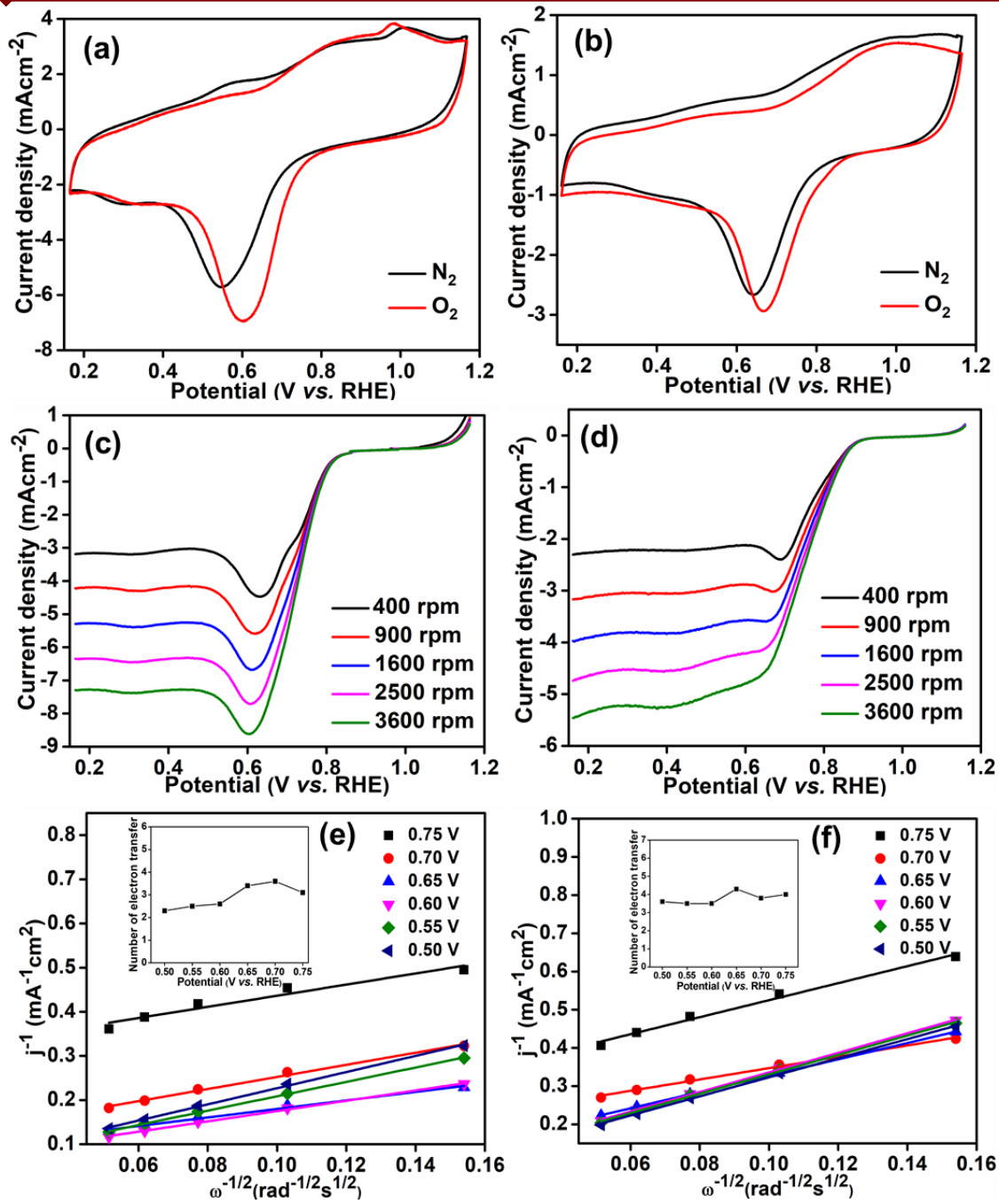

Figure 3.8: Electrochemical characterization of the catalysts: (a,b) CV curves of Pd_3Cu/C and $PdCu_3/C$ in 0.1 M KOH with N_2 and O_2 saturated atmosphere, (c,d) LSV curves of Pd_3Cu/C and $PdCu_3/C$ at 400-3600 rpm, and (e,f) corresponding KL plot of Pd_3Cu/C and $PdCu_3/C$ (inset: electron transfer number at different potentials).

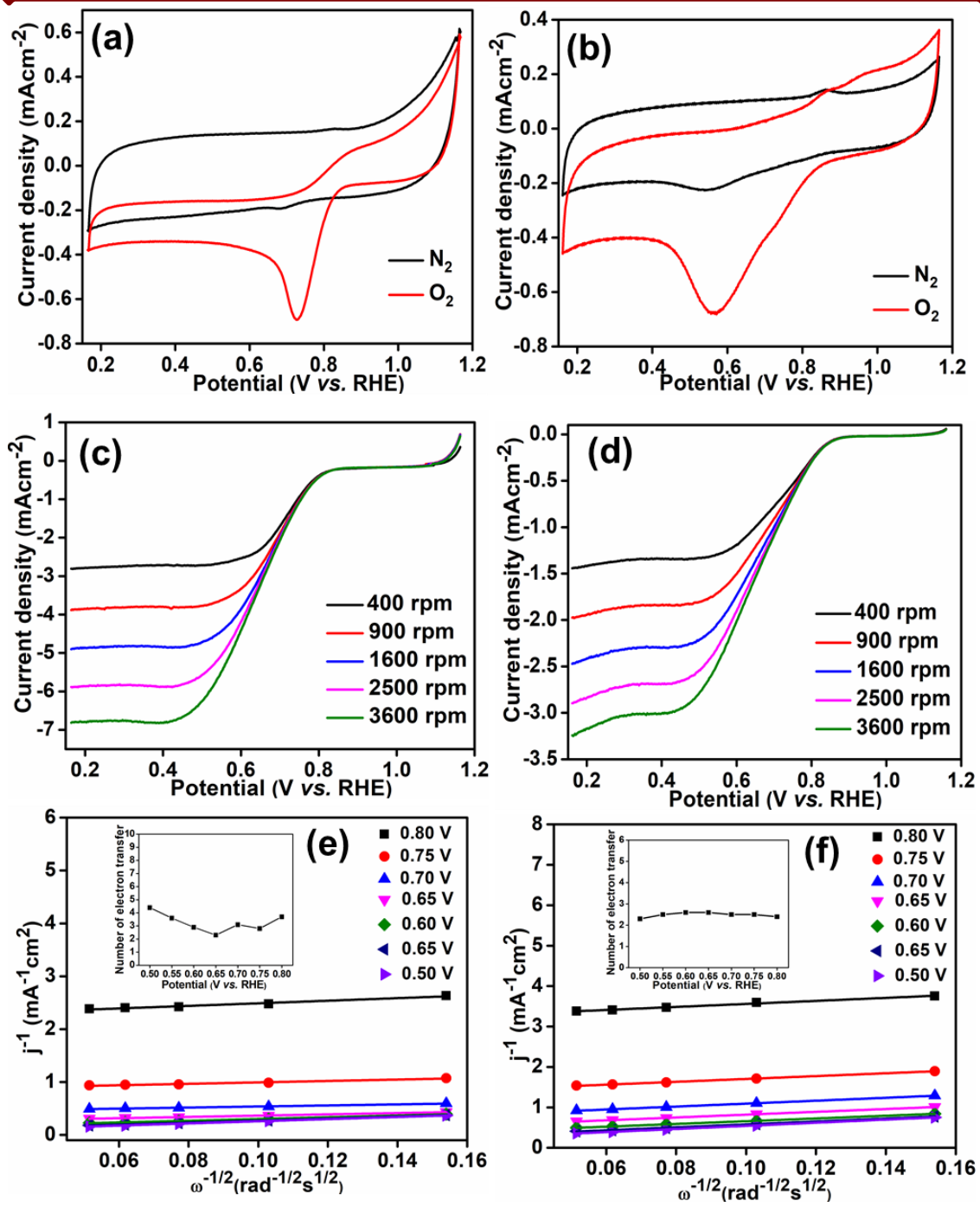

Figure 3.9: Electrochemical characterization of the catalysts: (a,b) CV curves of Pd_3Ag/C and $PdAg_3$/C in 0.1 M KOH with N_2 and O_2 saturated atmosphere, (c,d) LSV curves of Pd_3Ag/C and $PdAg_3$/C at 400-3600 rpm, and (e,f) corresponding KL plot of Pd_3Ag/C and $PdAg_3$/C (inset: electron transfer number at different potentials).

In addition, the electrochemical surface areas (ECSAs) of the electrocatalysts were also calculated and it is an important factor for evaluating the catalytically active sites of the electrocatalysts [3, 40]. The ECSA is measured by conducting CV in N_2 saturated environment and CV plot of all the electrocatalysts presented in Figure 3.10a. The calculation method of ECSA has already been discussed in Chapter 2. The ECSAs are calculated to be $Pd_3Ag_{0.5}Cu_{0.5}$/C (146.5 m^2g^{-1}), Pd_3Ag/C (2.08 m^2g^{-1}), Pd_3Cu/C (137.3 m^2g^{-1}), $PdAg_3$/C (4.1 m^2g^{-1}), $PdCu_3$/C (66.2 m^2g^{-1}) and Pt/C NPs (26.5 m^2g^{-1}). As expected, $Pd_3Ag_{0.5}Cu_{0.5}$/C has higher ECSA and the higher ECSA of $Pd_3Ag_{0.5}Cu_{0.5}$/C signifies the presence of more active sites, increasing their ORR activity. The ECSA specific ORR activity of the electrocatalysts, which is normalized by the ECSA surface area, is shown in Figure 3.10b.

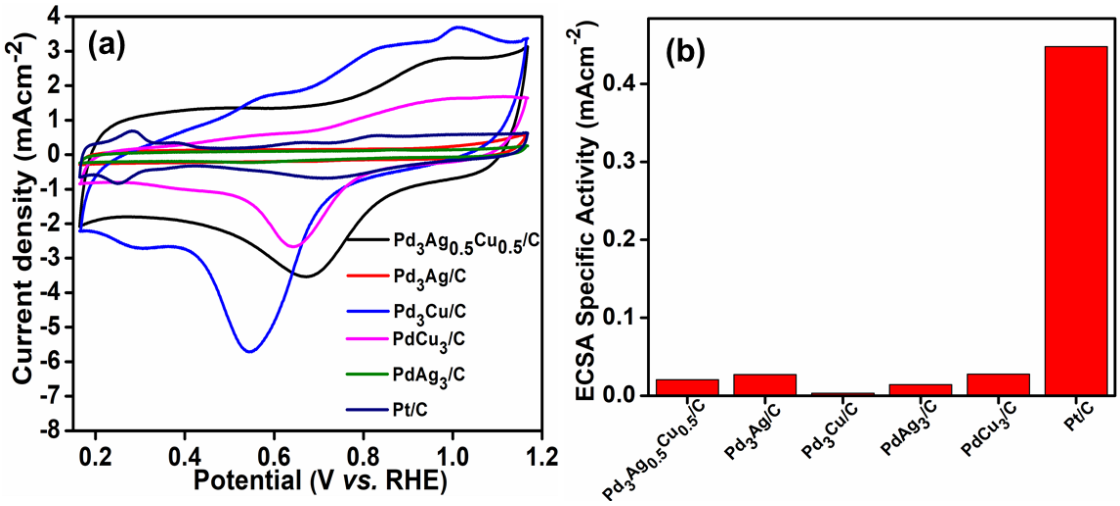

Figure 3.10: (a) CV curves of $Pd_3Ag_{0.5}Cu_{0.5}$/C, Pd_3Cu/C, Pd_3Ag/C, $PdAg_3$/C, $PdCu_3$/C and Pt/C in 0.1 M KOH with N_2-saturated atmosphere and (b) ECSA specific activity of $Pd_3Ag_{0.5}Cu_{0.5}$/C, Pd_3Cu/C, Pd_3Ag/C, $PdAg_3$/C, $PdCu_3$/C and Pt/C.

The Tafel slope of $Pd_3Ag_{0.5}Cu_{0.5}$/C Pd_3Cu/C, Pd_3Ag/C, $PdAg_3$/C and $PdCu_3$/C in Figure 3.11a obtained from the potential (V) versus log of current density plots (log j_k) from their corresponding LSV plots reveals insight into the ORR kinetics. The $Pd_3Ag_{0.5}Cu_{0.5}$/C exhibits the Tafel slope of 78.5 $mVdec^{-1}$ which is lower than the Pd_3Ag/C (123.8 $mVdec^{-1}$), Pd_3Cu/C (93.7 $mVdec^{-1}$) $PdCu_3$/C (80.3 $mVdec^{-1}$) and $PdAg_3$/C (85.8 $mVdec^{-1}$) implying faster ORR kinetics [3, 37-39].

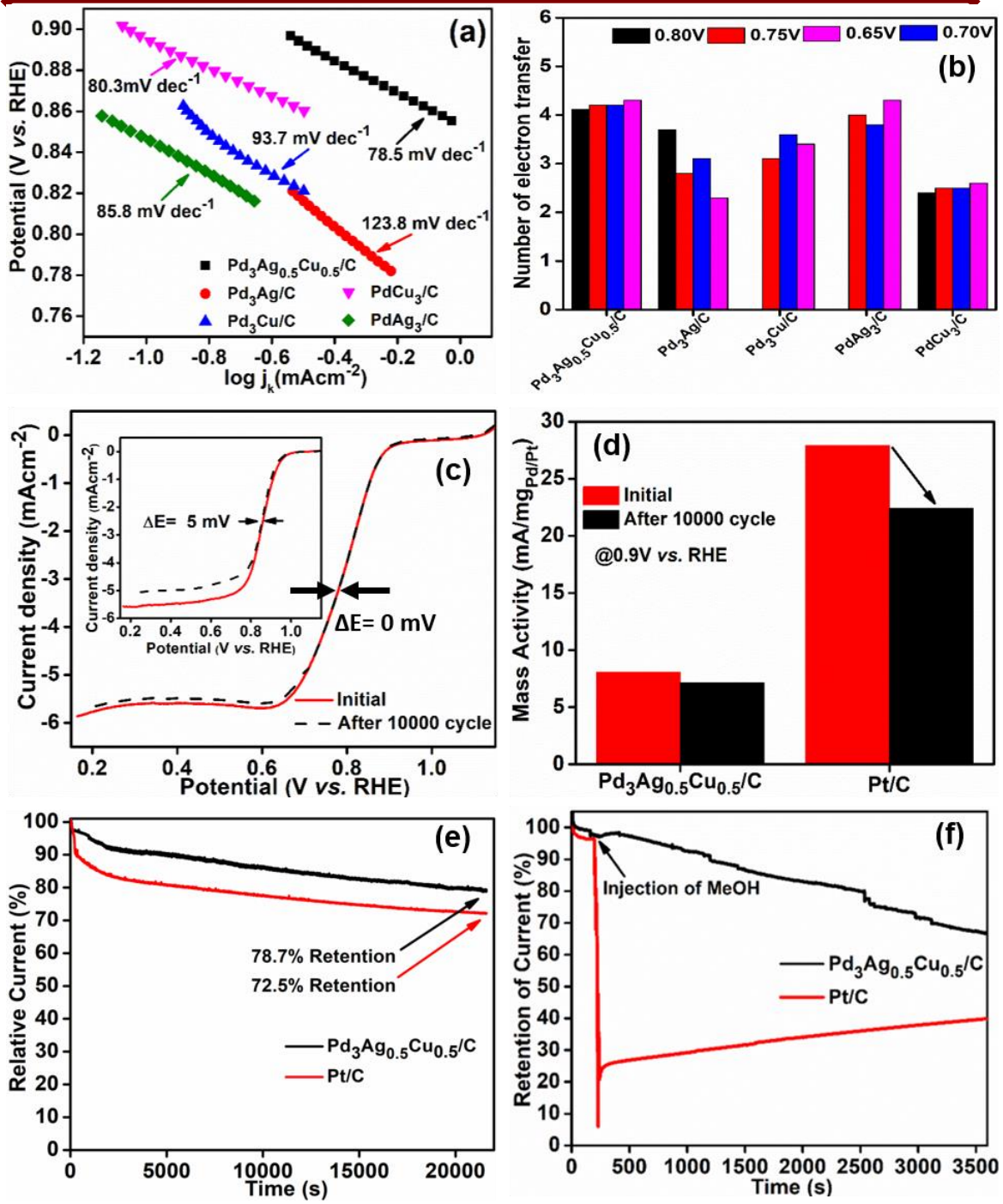

Figure 3.11: (a) Tafel plot for $Pd_3Ag_{0.5}Cu_{0.5}$/C, Pd_3Cu/C, Pd_3Ag/C, $PdAg_3$/C and $PdCu_3$/C, (b) electron transfer number of $Pd_3Ag_{0.5}Cu_{0.5}$/C, Pd_3Cu/C, Pd_3Ag/C, $PdAg_3$/C and $PdCu_3$/C at different potentials, (c) LSV curves of $Pd_3Ag_{0.5}Cu_{0.5}$/C and Pt/C before and after 10,000 CVs in 0.1M KOH, (d) mass specific activity of $Pd_3Ag_{0.5}Cu_{0.5}$/C and Pt/C before and after ADT in 0.1M KOH, (e) CA of $Pd_3Ag_{0.5}Cu_{0.5}$/C and Pt/C for 21600 s and (f) MeOH tolerance test of $Pd_3Ag_{0.5}Cu_{0.5}$/C and Pt/C.

A challenge confronting the advancement of FCs catalysts is their inadequate operational stability and durability. Thus, one of this research's primary goals is to improve the stability and durability of the electrocatalysts. We then evaluated their long-term ADTs; the ADTs of $Pd_3Ag_{0.5}Cu_{0.5}$/C and commercial Pt/C were tested in O_2-saturated 0.1M KOH electrolyte within the potential window of 0.55-0.95 V *vs.* RHE for 10000 cycles. The LSV curves in Figure 3.11c reveal no attenuation in $E_{1/2}$ and E_{onset}, whereas for Pt/C a slight shift is observed in $E_{1/2}$ after 10000 consecutive cycles. In addition, there is slight loss in MA after 10000 ADT operations, whereas for Pt/C a significant loss of initial value was observed (Figure 3.11d). To test the electrostability of the catalyst we did the CA test at 0.53V *vs.* RHE for 21,600 s. At the end of 21,600 s continuous operations, our ternary catalysts retain ~79% of the initial current; in stark contrast, Pt/C retains 72.5% (Figure 3.11e).

It is well known that FCs face a significant challenge when it comes to ORR catalysts' methanol tolerance since methanol permeability into the cathode side significantly reduces the efficiency of FCs. Thus, CA measurement was used to assess the impact of methanol tolerance of $Pd_3Ag_{0.5}Cu_{0.5}$/C in an O_2-saturated 0.1M KOH solution containing 0.1M methanol. As presented in Figure 3.11f, the $Pd_3Ag_{0.5}Cu_{0.5}$/C did not significantly alter after adding methanol. On the other hand, a significant change is observed when MeOH is added in the case of commercial Pt/C. So, we can say that $Pd_3Ag_{0.5}Cu_{0.5}$/C is a potentially useful catalyst for direct methanol fuel cells (DMFCs), as evidenced by the stability of the methanol tolerance test. The synthesized electrocatalysts exhibit markedly improved stability and durability over commercial electrocatalysts primarily because of the encapsulating effect of high surface area carbon support and the electronic interaction among Pd, Ag and Cu atoms.

We further studied the variations of the morphology, crystal structure and chemical composition of $Pd_3Ag_{0.5}Cu_{0.5}$/C after the stability tests. No obvious change in the structure and morphology of the $Pd_3Ag_{0.5}Cu_{0.5}$/C catalyst was observed, indicating its excellent stability. The high-resolution XPS spectra of Pd 3d, Cu 2p, Ag 3d, and C 1s from $Pd_3Ag_{0.5}Cu_{0.5}$/C after CA are presented in Figure 3.12. In the XPS spectrum of these atoms we have slight changes in binding energy after the stability test, revealing that electrons transferred to molecular O_2 from the catalyst's surface during the reaction. The binding energy comparison values Pd $3d_{5/2}$, Ag $3d_{5/2}$ and Cu $2p_{3/2}$ of $Pd_3Ag_{0.5}Cu_{0.5}$/C before and after the CA test presented in Table 3.3. Moreover, the morphology of the

$Pd_3Ag_{0.5}Cu_{0.5}$/C remains intact with no obvious particle growth and agglomeration (Figure 3.13). We observed a beautiful dispersion of metal NPs over carbon support after this long hour test. The HRTEM in Figure 3.13c reveals that the clear lattice fringes with the d-spacing of ~ 0.219, 0.204, 0.236 nm, indexed to Pd(111), Ag(111) and Cu(111) plane. The distribution histogram (Figure 3.13d) reveals that the diameter of $Pd_3Ag_{0.5}Cu_{0.5}$ is within the size range of 2−12 nm and the average size of 6 nm.

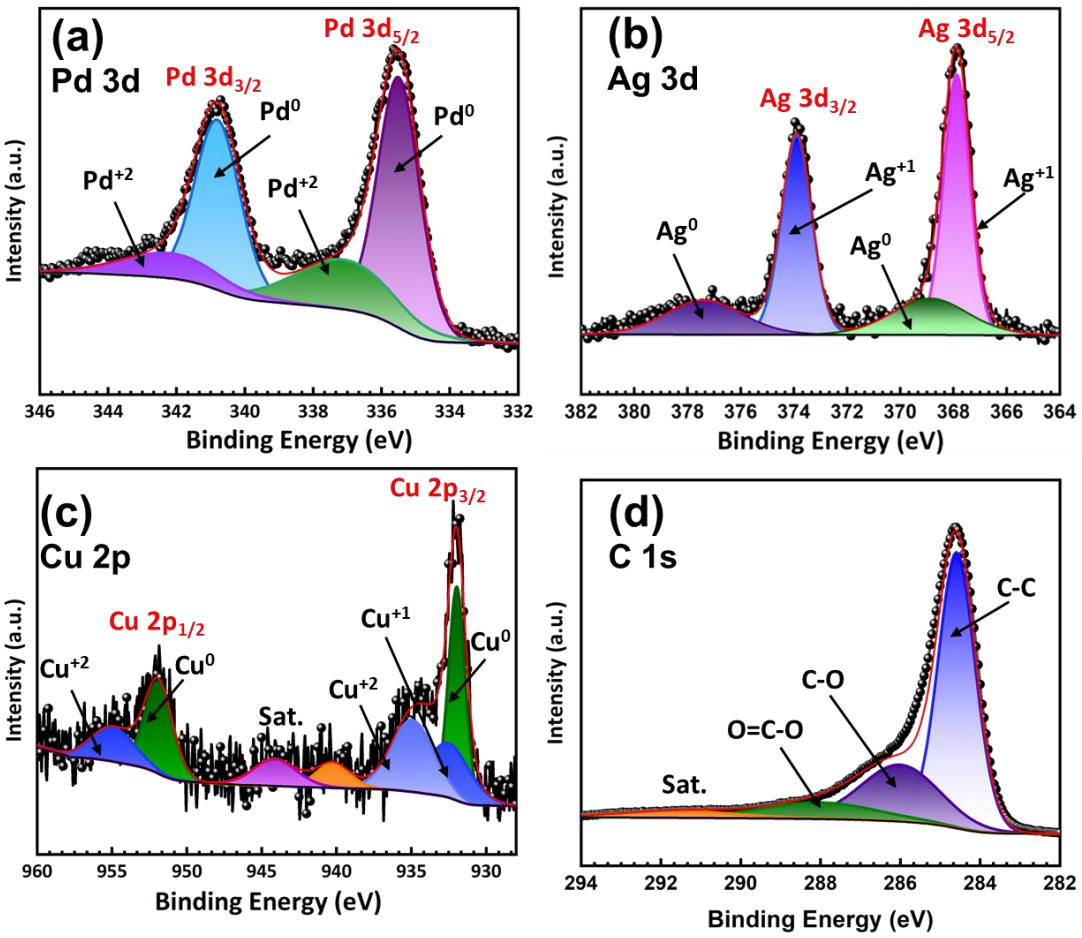

Figure 3.12: High resolution XPS spectra of (a) Pd 3d, (b) Ag 3d, (c) Cu 2p, and (d) C 1s of $Pd_3Ag_{0.5}Cu_{0.5}$/C after CA test.

Table 3.3: Comparison of BE Pd $3d_{5/2}$, Ag $3d_{5/2}$ and Cu $2p_{3/2}$ of $Pd_3Ag_{0.5}Cu_{0.5}$/C before and after CA test

	Pd $3d_{5/2}$	**Ag $3d_{5/2}$**	**Cu $2p_{3/2}$**
Before CA	335.3 eV	368.0 eV	932.1 eV
After CA	335.5 eV	368.1 eV	932.3 eV

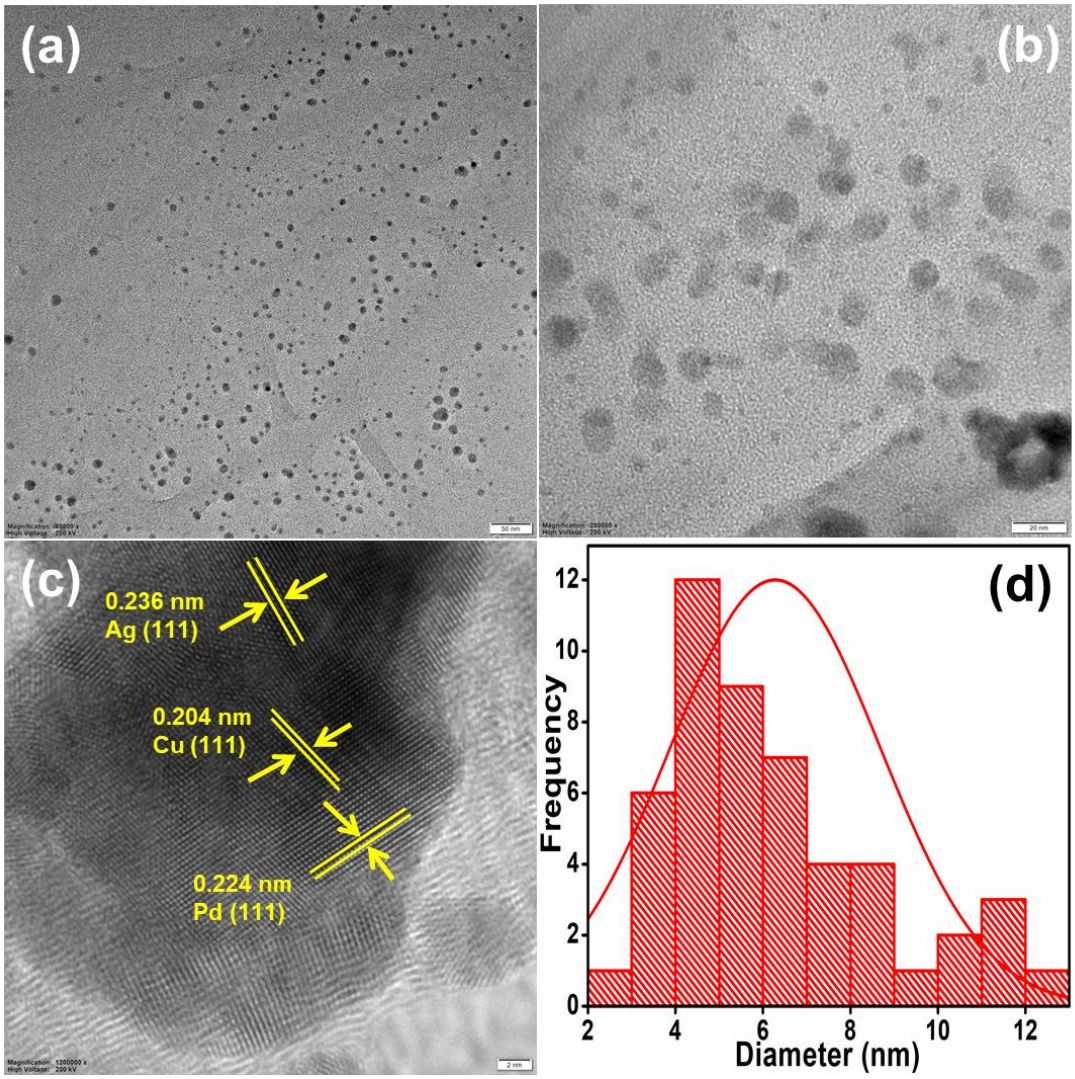

Figure 3.13: (a,b) Transmission electron microscopy (TEM) image, (c) high-resolution TEM (HRTEM) image, (d) plot distributions histogram of $Pd_3Ag_{0.5}Cu_{0.5}/C$ measured from the image (a) after CA test.

From the above findings, we can say that $Pd_3Ag_{0.5}Cu_{0.5}/C$ exhibits remarkable catalytic performance and durability toward ORR, which is significantly correlated with uniform distribution on the graphene support and trimetallic characteristics. The uniform distribution of metal NPs on the graphene surface offers reduced diffusion resistance and fast mass transfer, enhancing catalytically active sites and ECSA. Trimetallic structure can modify the electronic structure of each metal, which helps to enhance the interaction between the oxygenated intermediate and active sites, therefore improving the ORR efficiency [41-43]. Incorporating Pd with Ag and Cu causes the lattice contraction of Pd and the downward shifting of the *d*-band center of Pd. According to density functional

theory (DFT), the *d*-band center of the catalysts is strongly related to the changes in the catalyst surface binding energy and the intermediates adsorbed on the surface. The upper position of the *d*-band with respect to the Fermi level indicates stronger interactions with the oxygenated adsorbates. Pd exhibits stronger interactions with oxygen at a faster kinetic rate for the breaking of O-O bonds than those exhibited by oxygen bond making, which indicates slower kinetics for the ORR. Thus, the kinetics of the ORR may be enhanced by altering the d-band center for Pd by adding second or third metals into the Pd lattice.

Table 3.4: Comparison of the ORR parameters of Pd-based electrocatalysts in 0.1 M KOH

Electrocatalysts	**E_{onset} V (*vs.* RHE)**	**$E_{1/2}$ V (*vs.* RHE)**	**ECSA (m^2g^{-1})**	**References**
$Pd_3Ag_{0.5}Cu_{0.5}$/C	0.94	0.80	146.5	This work
PBA-Pd-Co/C	0.91	0.82	46.82	42
e-Pt_1Pd_1/rGO	-	0.934	125.5	43
Pd@PdO-Co_3O_4	0.923	0.727	-	44
N-rGO-Pd	0.91	0.76	85.34	45
10% Pd/MnO_2	0.866	0.780		46
Pd NPAs	0.926	0.837	34.968	47
$Au_{67}Pd_{33}$/CN	0.94	0.83	70.1	48
PdNiMnO-PF	0.94	0.84	81.9	49

Interestingly, the ORR performance of $Pd_3Ag_{0.5}Cu_{0.5}$/C is superior or comparable to the most recently published Pd-based electrocatalysts under the identical electrochemical test conditions. The comparison results are tabulated in Table 3.4. It is observed that the E_{onset} and $E_{1/2}$ of $Pd_3Ag_{0.5}Cu_{0.5}$/C superior than with that of PBA-Pd-Co/C [42], Pd@PdO-Co_3O_4 [44], N-rGO-Pd [45], 10% Pd/MnO_2 [46], Pd NPAs [47] and comparable to $Au_{67}Pd_{33}$/CN [48], PdNiMnO-PF [49] in 0.1M KOH solution. The

$Pd_3Ag_{0.5}Cu_{0.5}$/C electrocatalyst also exhibited a larger ECSA value, outperforming all of the reported catalysts, indicating the existence of abundant active surface area. From the above comparison, we can say that the catalyst obtained by incorporating Ag and Cu into the Pd lattice displayed the best electrocatalytic performance for ORR in alkaline media.

3.3. Conclusions

In summary, a highly stable and durable $Pd_3Ag_{0.5}Cu_{0.5}$/C electrocatalyst with homogenous dispersion was synthesized, which exhibits remarkable stability and durability and excellent MeOH tolerance. The electrochemical measurement, including CV and LSV analyses, demonstrates that $Pd_3Ag_{0.5}Cu_{0.5}$/C performs better than the other electrocatalysts in terms of its superior limiting current density, early E_{onset} and $E_{1/2}$. Additionally, the remarkable long-term electrostability and durability as well as excellent tolerance to MeOH are evident in its excellent tolerance to agglomeration and minute deactivation rates, as seen in CA and ADT. The presence of Ag and Cu metals tune the electronic structure of Pd due to the synergistic effect among them and weakens the Pd-adsorbate binding energy, promoting the ORR process. Furthermore, the graphene support plays a crucial role by improving the dispersion of nanoparticles and enhancing the metal−support interaction. This work provides a new protocol to construct non-Pt electrocatalysts and opens new avenues for the application of stable and durable nanomaterials in high-efficiency ORR electrocatalysts.

References

[1] Verma, S., Lu, S., Kenis, P.J. Co-electrolysis of CO_2 and glycerol as a pathway to carbon chemicals with improved technoeconomics due to low electricity consumption. *Nature Energy*, 4(6):466-474, 2019.

[2] Garcia, A.C., Caliman, J., Ferreira, E.B., Tremiliosi-Filho, G., Linares, J.J. Promotional effect of Ag on the catalytic activity of Au for glycerol electrooxidation in alkaline medium. *ChemElectroChem*, 2(7):1036-1041, 2015.

[3] Chetry, R., Chutia, B., Patowary, S., Borah, B.J., Sudarsanam, P., Bharali, P. Electronic modulation of Pd/C by simultaneous doping of Cu and Co tendering a highly durable and methanol-tolerant oxygen reduction electrocatalyst. *Energy & Fuels*, 37(13):9557-9567, 2023.

[4] Kumar, R., Singh, R. and Dutta, S. Review and outlook of hydrogen production

through catalytic processes. *Energy & Fuels*, 38(4):2601-2629, 2024.

[5] Chen, M., Luo, L., Wu, C., Wang, B., Zhou, S., Wang, Q. Morphology engineering of self-assembled bimetallic PtCo alloy nanofoams as efficient multifunctional electrocatalysts for oxygen reduction and alcohol oxidation. *Applied Surface Science*, 657:159833, 2024.

[6] Zhu, W., Yuan, H., Liao, F., Shen, Y., Shi, H., Shi, Y., Xu, L., Ma, M., Shao, M. Strain engineering for janus palladium-gold bimetallic nanoparticles: Enhanced electrocatalytic performance for oxygen reduction reaction and zinc-air battery. *Chemical Engineering Journal*, 389:124240, 2020.

[7] Lin, J. Y., Xi, C., Li, Z., Feng, Y., Wu, D. Y., Dong, C. K., Yao, P., Liu, H., Du, X. W. Lattice-strained palladium nanoparticles as active catalysts for the oxygen reduction reaction. *Chemical Communications*, 55:3121−3123, 2019.

[8] Liu, F., Liu, Y., Gao, D., Ma, S., Zhang, S., Li, Y., Zhang, J., Xue, Y.,Tang, C. Designing a MnF_2/MnO_2 heterostructure for enhanced electrocatalysis in the oxygen reduction reaction. *Colloids and Surfaces A: Physicochemical and Engineering*, 688:133637, 2024.

[9] Roy, N., Yasmin, S., Ejaz, A., Han, H. S., Jeon, S. Influence of pyrrolic and pyridinic-N in the size and distribution behaviour of Pd nanoparticles and ORR mechanism. *Applied Surface Science*, 533:147500, 2020.

[10] Wang, Q., Guesmi, H., Tingry, S., Cornu, D., Holade, Y.,Minteer, S.D. Unveiling the pitfalls of comparing oxygen reduction reaction kinetic data for Pd-based electrocatalysts without the experimental conditions of the current–potential curves. *ACS Energy Letters*, 7(3):952-957, 2022.

[11] Wang, H., Zhou, T., Xu, S., Deng, K., Yu, H., Xu, Y., Li, X., Wang, Z., Wang, L. Boron-intercalation-triggered crystalline transition of Pd nanosheet assemblies for an enhanced oxygen reduction reaction. *Nanotechnology*, 35(15):155401, 2024.

[12] Qin, Z., Wang, T., Yao, Z., Li, Q. Unconventional intermetallic noble metal nanocrystals for energy-conversion electrocatalysis. *EES Catalysis*, 2:545-555, 2024.

[13] Guan, J., Dong, D., Khan, N.A., Zheng, Y. Emerging Pt-based intermetallic nanoparticles for the oxygen reduction reaction. *Chemical Communications*, 60(14):1811-1825, 2024.

[14] Wang, Q., Cai, J., Sun, Y., Chen, W., Huang, H., Wang, S., Fu, L., Xie, S. Urchin-

like Au/Pd nanobranches for the oxygen reduction electrocatalysis. *ACS Applied Nano Materials*, 7(5):5534-5542, 2024.

[15] Fernandez, J. L., Walsh, D. A., Bard, A. J. Thermodynamic guidelines for the design of bimetallic catalysts for oxygen electro reduction and rapid screening by scanning electrochemical microscopy. M−Co (M: Pd, Ag, Au). *Journal of the American Chemical Society*, 127:357–365, 2005.

[16] Stamenkovic, V. R., Fowler, B., Mun, B. S., Wang, G., Ross, P. N., Lucas, C. A., Markovic, N. M. Improved oxygen reduction activity on $Pt_3Ni(111)$ via increased surface site availability, *Science*, 315:493–497, 2007.

[17] Koh, S., Strasser, P. Electrocatalysis on bimetallic surfaces: Modifying catalytic reactivity for oxygen reduction by voltammetric surface dealloying. *Journal of the American Chemical Society*, 129:12624–12625, 2007.

[18] Savadogo, O., Lee, K., Oishi, K., Mitsushima, S., Kamiya, N., Ota, K. I. New palladium alloys catalyst for the oxygen reduction reaction in an acid medium. *Electrochemistry Communications*, 6:105–109, 2004.

[19] Shao, M.H., Huang, T., Liu, P., Zhang, J., Sasaki, K., Vukmirovic, M.B., Adzic, R.R. Palladium monolayer and palladium alloy electrocatalysts for oxygen reduction. *Langmuir*, 22(25):10409-10415, 2006.

[20] Tang, W., Zhang, L., Henkelman, G. Catalytic activity of Pd/Cu random alloy nanoparticles for oxygen reduction. *The Journal of Physical Chemistry Letters*, 2(11):1328-1331, 2011.

[21] Wu, T., Sun, M., Huang, B. Atomic-strain mapping of high-index facets in late-transition-metal nanoparticles for electrocatalysis. *Angewandte Chemie International Edition*, 60(42):22996-23001, 2021.

[22] Quesnel, E., Roux, F., Emieux, F., Faucherand, P., Kymakis, E., Volonakis, G., Giustino, F., Martín-García, B., Moreels, I., Gürsel, S.A., Yurtcan, A.B. Graphene-based technologies for energy applications, challenges and perspectives. *2D Materials*, 2(3):030204, 2015.

[23] Daş, E., Gürsel, S.A., Şanli, L.I., Yurtcan, A.B. Comparison of two different catalyst preparation methods for graphene nanoplatelets supported platinum catalysts. *International Journal of Hydrogen Energy*, 41(23):9755-9761, 2016.

[24] Daş, E., Gürsel, S.A., Şanlı, L.I., Yurtcan, A.B. Thermodynamically controlled Pt deposition over graphene nanoplatelets: Effect of Pt loading on PEM fuel cell

performance. *International Journal of Hydrogen Energy*, 42(30):19246-19256, 2017.

[25] Karuppasamy, L., Anandan, S., Chen, C.Y., Wu, J.J. Sonochemical synthesis of PdAg/RGO nanocomposite as an efficient electrocatalyst for both ethanol oxidation and oxygen reduction reaction with high CO tolerance. *Electrocatalysis*, 8:430-441, 2017.

[26] Ge, X., Guan, Q., Zhang, F., Sun, S., Xu, Y., Zhang, K., Yuan, W., Zhang, L.Y. Direct epitaxial growth of Au nanoparticles on Pd metallene enables robust oxygen reduction electrocatalysis. *Materials Today Energy*, 39:101471, 2024.

[27] Feng, G., Ning, F., Song, J., Shang, H., Zhang, K., Ding, Z., Gao, P., Chu, W. and Xia, D. Sub-2 nm ultrasmall high-entropy alloy nanoparticles for extremely superior electrocatalytic hydrogen evolution. *Journal of the American Chemical Society*, 143(41):17117-17127, 2021.

[28] Zhang, Y., Huang, B., Shao, Q., Feng, Y., Xiong, L., Peng, Y. and Huang, X. Defect engineering of palladium–tin nanowires enable efficient electrocatalysts for fuel cell reactions. *Nano Letters*, 19(10):6894-6903, 2019.

[29] Adhikary, R., Sarkar, D., Mukherjee, M. and Datta, J. Remarkable performance of the unique Pd–Fe_2O_3 catalyst towards EOR and ORR: Non-Pt and non-carbon electrode materials for low-temperature fuel cells. *Journal of Materials Chemistry A*, 9(5):3052-3065, 2021.

[30] Li, W., Bhuvanendran, N., Zhang, W., Xu, Q., Hooshyari, K. and Su, H. Multi-skeletal PtPdNi nanodendrites as efficient electrocatalyst with high activity and durability towards oxygen reduction reaction. *International Journal of Hydrogen Energy*, 47(59):24807-24816, 2022.

[31] Zhang, S., Mo, Z., Wang, J., Liu, H., Liu, P., Hu, D., Tan, T. and Wang, C. Ultra-stable oxygen species in Ag nanoparticles anchored on g-C_3N_4 for enhanced electrochemical reduction of CO_2. *Electrochimica Acta*, 390:138831, 2021.

[32] Ruiz-Camacho, B., Medina-Ramírez, A., Fuentes-Ramírez, R., Navarro, R., Goméz, C.M. and Pérez-Larios, A. Pt and Pt–Ag nanoparticles supported on carbon nanotubes (CNT) for oxygen reduction reaction in alkaline medium. *International Journal of Hydrogen Energy*, 47(70):30147-30159, 2022.

[33] Solomon, G., Kohan, M.G., Vagin, M., Rigoni, F., Mazzaro, R., Natile, M.M., You, S., Morandi, V., Concina, I. and Vomiero, A. Decorating vertically aligned

MoS_2 nanoflakes with silver nanoparticles for inducing a bifunctional electrocatalyst towards oxygen evolution and oxygen reduction reaction. *Nano Energy*, 81:105664, 2021.

[34] Yu, Y., Dong, X.A., Chen, P., Geng, Q., Wang, H., Li, J., Zhou, Y. and Dong, F. Synergistic effect of Cu single atoms and Au–Cu alloy nanoparticles on TiO_2 for efficient CO_2 photoreduction. *ACS Nano*, 15(9):14453-14464, 2021.

[35] Song, T., Xue, H., Sun, J., Guo, N., Sun, J. and Wang, Q. Solvent assistance induced surface N-modification of PtCu aerogels and their enhanced electrocatalytic properties. *Chemical Communications*, 57(58):7140-7143, 2021.

[36] He, X., Long, X., Wang, P., Wu, H., Han, P., Tang, Y., Li, K., Ma, X. and Zhang, Y. Interconnected 3D Fe_3O_4/rGO as highly durable electrocatalyst for oxygen reduction reaction. *Journal of Alloys and Compounds*, 855:157422, 2021.

[37] Wang, Z., Jin, X., Chen, F., Bian, S., Li, J. and Chen, J. Construction of Pt/powder charcoal electrocatalyst utilizing MnO_2 as an additive to improve the stability for oxygen reduction reaction. *ACS Applied Engineering Materials*, 1(3):1024-1033, 2023.

[38] Tabari, T., Kobielusz, M., Singh, D., Yu, J. and Macyk, W. Cobalt-/copper-containing perovskites in oxygen evolution and reduction reactions. *ACS Applied Engineering Materials*, 1(8):2207-2216, 2023.

[39] Ling, L.L., Liu, W.J., Chen, S.Q., Hu, X. and Jiang, H. MOF templated nitrogen doped carbon stabilized Pt–Co bimetallic nanoparticles: Low Pt content and robust activity toward electrocatalytic oxygen reduction reaction. *ACS Applied Nano Materials*, *1*(7):3331-3338, 2018.

[40] Zhang, L.Y., Meng, X., Zhang, W., Zeng, T., Yuan, W. and Zhao, Z. Synthesis of palladium–tungsten metallene-constructed sandwich-like nanosheets as bifunctional catalysts for direct formic acid fuel cells. *ACS Applied Energy Materials*, 4(11):12336-12344, 2021.

[41] Huang, W., Wang, H., Zhou, J., Wang, J., Duchesne, P.N., Muir, D., Zhang, P., Han, N., Zhao, F., Zeng, M. and Zhong, J. Highly active and durable methanol oxidation electrocatalyst based on the synergy of platinum–nickel hydroxide–graphene. *Nature Communications*, 6(1):1-8, 2015.

[42] Liu, X., Han, J., Deng, J., Imhanria, S., Ren, Z. and Wang, W. Prussian blue analogue derived Pd-Co composite bifunctional electrocatalyst for Zn–air

battery. *Journal of Alloys and Compounds*, 832:154896, 2020.

[43] Ma, G., Zhao, X., Wang, J., Qin, G., Lu, Z., Yu, X., Li, L., Zhang, X. and Yang, X. The alloying effect of PtPd/rGO and the improvement of its ORR performance. *Catalysis Letters*, 154(5):2162-2170, 2024.

[44] Li, H.C., Zhang, Y.J., Hu, X., Liu, W.J., Chen, J.J. and Yu, H.Q., Metal–organic framework templated Pd@PdO–Co_3O_4 nanocubes as an efficient bifunctional oxygen electrocatalyst. *Advanced Energy Materials*, 8(11):1702734, 2018.

[45] Wu, X.T., Li, J.C., Pan, Q.R., Li, N. and Liu, Z.Q., Gallic acid-assisted synthesis of Pd uniformly anchored on porous N-rGO as efficient electrocatalyst for microbial fuel cells. *Dalton Transactions*, 47(5): 1442-1450, 2018.

[46] Cruz-Reyes, I., Trujillo-Navarrete, B., García-Tapia, K., Salazar-Gastélum, M.I., Paraguay-Delgado, F., Félix-Navarro, R.M. Pd/MnO_2 as a bifunctional electrocatalyst for potential application in alkaline fuel cells. *Fuel*, 279:118470, 2020.

[47] Liu, S., Mu, X., Duan, H., Chen, C. and Zhang, H., 2017. Pd nanoparticle assemblies as efficient catalysts for the hydrogen evolution and oxygen reduction reactions. *European Journal of Inorganic Chemistry*, (3):535-539, 2017.

[48] Yan, W., Tang, Z., Wang, L., Wang, Q., Yang, H. and Chen, S., PdAu alloyed clusters supported by carbon nanosheets as efficient electrocatalysts for oxygen reduction. *International Journal of Hydrogen Energy*, 42(1):218-227, 2017.

[49] Zhang, W., Chang, J., Wang, G., Li, Z., Wang, M., Zhu, Y., Li, B., Zhou, H., Wang, G., Gu, M. and Feng, Z., Surface oxygenation induced strong interaction between Pd catalyst and functional support for zinc–air batteries. *Energy & Environmental Science*, 15(4):1573-1584, 2022.